Earth and Planetary Science Letters 286 (2009) 467–478

Contents lists available at ScienceDirect

Earth and Planetary Science Letters

journal homepage: www.elsevier.com/locate/epsl

The late Quaternary slip-rate of the Har-Us-Nuur fault (Mongolian Altai) from cosmogenic ^{10}Be and luminescence dating

Edwin Nissen [a,*,1], Richard T. Walker [a], Amgalan Bayasgalan [b], Andrew Carter [c], Morteza Fattahi [d,e], Erdenebat Molor [b], Christoph Schnabel [f], A. Joshua West [a], Sheng Xu [g]

[a] Centre for the Observation and Modelling of Earthquakes and Tectonics (COMET), Department of Earth Sciences, University of Oxford, Parks Road, Oxford OX1 3PR, UK
[b] Mongolian University of Science and Technology, Ulaan Bataar, Mongolia
[c] School of Earth Sciences, Birkbeck College, London WC1E 7HX, UK
[d] Oxford University Centre for the Environment, South Parks Road, Oxford OX1 3QY, UK
[e] Institute of Geophysics, Tehran University, Kargar Shomali, Tehran, Iran
[f] NERC Cosmogenic Isotope Analysis Facility, East Kilbride G75 0QF, UK
[g] Scottish Universities Environmental Research Centre, East Kilbride G75 0QF, UK

ARTICLE INFO

Article history:
Received 18 November 2008
Received in revised form 16 June 2009
Accepted 30 June 2009
Available online 6 August 2009

Editor: T.M. Harrison

Keywords:
active tectonics
Altai
fault slip-rates
exposure dating
OSL dating

ABSTRACT

The Altai range (western Mongolia) accommodates NNE–SSW shortening across the northern India–Eurasia collision zone by dextral slip on faults trending NNW–SSE, and anticlockwise, vertical-axis rotations of fault-bounded blocks. However, fault slip-rates and the way in which faulting evolves over time are poorly understood, and form the motivation for this study. We focussed on the Har-Us-Nuur fault, a major transpressional fault bounding the eastern margin of the Altai. Three abandoned alluvial fan surfaces, each displaced right-laterally by the fault, were targeted for dating with cosmogenic ^{10}Be and quartz optically stimulated luminescence (OSL). The first surface (A2) shows an exponential decrease in ^{10}Be with increasing depth, with a significant inherited component. Modelling this profile yielded a minimum age of 74.1 ka. Material from the same sampling pit was dated at ~19 ka with OSL, but we consider this younger age to be incorrect, possibly due to feldspar contamination or abnormal quartz OSL characteristics. The A2 surface is displaced by 175 m, implying a (maximum) dextral slip-rate of 2.4 ± 0.4 mm yr^{-1}. A second fan surface (F1) was dated at ~6 ka with OSL and shows little variation in ^{10}Be with depth, consistent with this young age. The inherited component is higher than for A2, indicating contrasting levels of inheritance for different periods of fan aggradation. A final surface (F2) shows scattered ^{10}Be concentrations and lacks material suitable for OSL, so cannot be dated precisely. Using the total vertical displacement across the fault, we place the initiation of movement on the fault at ~2 Ma, significantly later than the late Oligocene to Miocene (28–5 Ma) onset of shortening in the Altai region. This suggests that deformation in the Altai has widened over time to incorporate new faults at the range margins (such as Har-Us-Nuur), possibly because older faults in the range interior have rotated about vertical axes into orientations that require work to be done against gravity.

1. Introduction

Late Quaternary fault slip-rates are important indicators of seismic hazard and provide valuable constraints for models of continental deformation. The collision between India and Eurasia is a key testing ground for these models (Avouac and Tapponnier, 1996; Peltzer and Saucier, 1996; England and Molnar, 1997; Holt et al., 2000; England and Molnar, 2005; Liu and Bird, 2008), but quantitative slip-rate data are primarily concentrated in the southern and central parts of this zone, in and around the Tibetan plateau (early papers include Van der Woerd et al., 1998; Lasserre et al., 1999; Brown et al., 2002) and the Tien Shan range (e.g. Burtman et al., 1996; Brown et al., 1998; Thompson et al., 2002). North of the Tien Shan such data become very sparse, with the notable exception of the Gobi-Altai region in southern Mongolia (Ritz et al., 1995; Owen et al., 1999; Ritz et al., 2003; Vassallo et al., 2005; Ritz et al., 2006; Vassallo et al., 2007).

This paper concerns the tectonics of the Mongolian-Altai range (henceforth termed the Altai), which forms the northernmost region of active shortening within the collision zone, around 2500 km north of the Himalaya (inset, Fig. 1a). The style of faulting and occurrence of large magnitude earthquakes in the Altai are well documented (e.g. Tapponnier and Molnar, 1979; Baljinnyam et al., 1993; Cunningham, 2005), but until now very little is known about how fast these faults move on late Quaternary time-scales, the frequency at which these large

* Corresponding author.
E-mail address: ed.nissen@earth.ox.ac.uk (E. Nissen).
[1] Present address: COMET, Bullard Laboratories, Department of Earth Sciences, University of Cambridge, Madingley Road, Cambridge CB3 0EZ, UK.

0012-821X/$ – see front matter © 2009 Elsevier B.V. All rights reserved.
doi:10.1016/j.epsl.2009.06.048

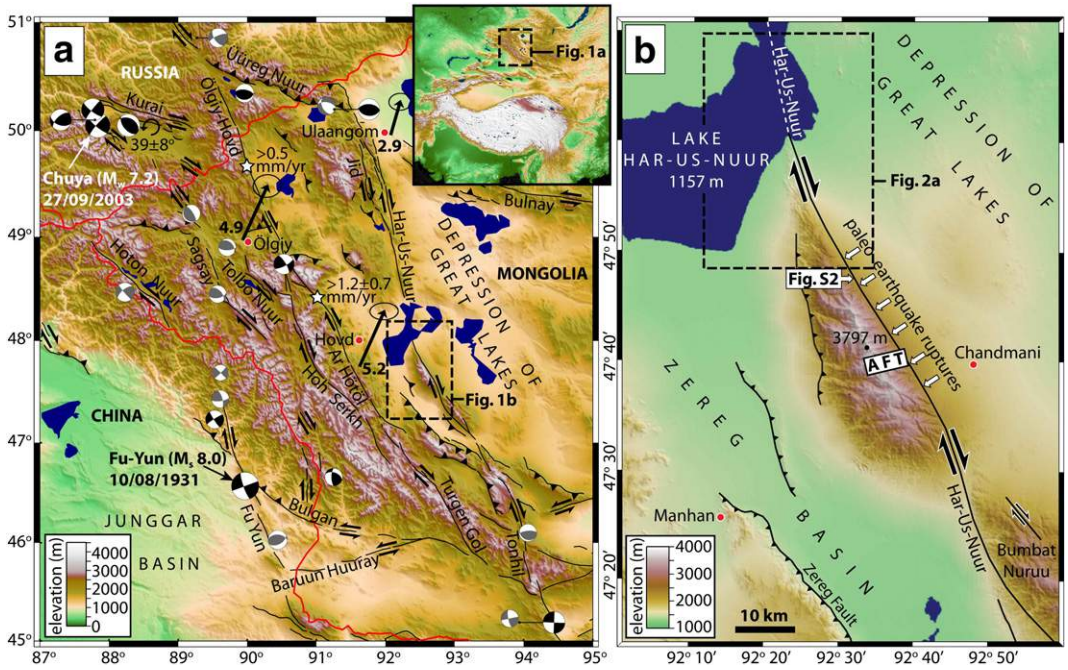

Fig. 1. (a) Earthquake focal mechanisms ($M_w \geq 5$), GPS vectors and active faults in the Altai mountains, plotted in a Mercator projection. Black focal mechanisms have been constrained with bodywave modelling or first motion polarities, and date from 1931 (Bayasgalan et al., 2005; Nissen et al., 2007). Grey mechanisms are from the Global CMT catalogue, 1977–2008 (for simplicity, six M_w 5.0–5.2 aftershocks of the 2003 Siberian Altai sequence are excluded). Earthquake epicentres are from the updated version of the Engdahl et al. (1998) catalogue. Arrows with bold numbers show GPS velocities (mm yr^{-1}) relative to stable Eurasia, with 95% confidence ellipses (Calais et al., 2003), while the curly arrow shows the location of paleomagnetic measurements of clockwise rotations in Neogene sediments in the NW Altai (Thomas et al., 2002). The two stars show the sites of Late Quaternary slip-rate estimates for the Ölgiy-Hovd fault (Vassallo, 2006). (b) Shuttle Radar Topography Mission (SRTM) topography and faulting around the Jargalant-Nuruu massif, displayed in the local UTM zone (46) projection (as are subsequent maps) and artificially illuminated from the NE. The extents of the paleo-earthquake ruptures described in the Appendix are indicated by white arrows, and the location of Fig. S2 is also shown. Apatite fission-track samples were taken from a transect of the Jargalant-Nuruu range covered by the white rectangle labelled AFT (see the Appendix).

events happen, or how the distribution of faulting has evolved through time. These questions are the motivation for this study.

We focus on the Har-Us-Nuur fault, a major, right-lateral strike-slip fault bounding the eastern margin of the Altai. The aim of the main part of the paper is to determine its late Quaternary slip-rate. To measure slip-rates accurately, robust ages and displacements of offset geomorphic markers must be determined. A number of techniques are available to date these landforms; the choice of which to use depends on the type, lithology and approximate age of the feature under consideration, and often only one is applicable at a particular site. As such, it is relatively uncommon for separate dating methods to be tested against one another. In this study, we determine the age of alluvial fans offset by the Har-Us-Nuur fault using both *in situ*-produced cosmogenic ^{10}Be and optically stimulated luminescence (OSL) dating. This is amongst the first, direct comparisons of these methods for dating alluvial fan deposits (Hetzel et al., 2004; Owen et al., 2006; DeLong and Arnold, 2007), and the first such study in Mongolia. By directly comparing the two methods, we can explore the uncertainties and limitations of each method in a way that would be impossible if one alone were used.

In the final part of the paper, we combine the Har-Us-Nuur slip-rate with the cumulative vertical displacement across the fault to estimate its age, and therefore the onset of deformation in the eastern Altai. Our results have significant implications for the evolution of faulting in an important part of the Alpine-Himalayan belt.

2. Tectonic setting

The Altai mountains are situated in western Mongolia and adjacent parts of China, Russia and Kazakhstan (Fig. 1a). According to GPS, the range accommodates ~7 mm yr^{-1} of NNE-directed shortening (Calais et al., 2003), a significant proportion of the total ~35–40 mm yr^{-1} India–Eurasia convergence, also constrained by GPS (e.g. Chen et al., 2000; Wang et al., 2001; Sella et al., 2002). The onset of India-related deformation in the Altai is poorly constrained; coarsening sedimentation in basins in and around the Altai points to initial range uplift during the late Oligocene or early Miocene (Devyatkin, 1974, 1981; Howard et al., 2003), whilst apatite fission-track (AFT) modelling suggests Pliocene in the Russian Altai (De Grave and Van den haute, 2002) and at the Baatar Hyarhan massif in the eastern Altai (Vassallo, 2006), but Miocene in the interior part of the Chinese Altai (Yuan et al., 2006).

In contrast with the Himalaya and Tien Shan to the south, where convergence is primarily accommodated by thrust faulting, shortening across the Altai is thought to be achieved by the anticlockwise vertical-axis rotations of N- to NW-trending dextral strike-slip faults (Baljinnyam et al., 1993; see also the schematic illustration in Fig. 9, Bayasgalan et al., 2005). This unusual style of convergence is probably influenced by the ~NW-trending structural grain of the Altai (Cunningham, 1998), which is inherited from the Palaeozoic accretion of continental fragments and arc terrain (Sengör et al., 1993). Many of the right-lateral faults include a significant reverse component, thus contributing to long-term range uplift. Peaks are up to 4.5 km in elevation and often distinctively flat-topped. These summit plateaus are remnants of a peneplain surface (Cunningham, 2001) which formed over much of central Asia during the Jurassic, according to AFT thermochronology (Jolivet et al., 2007).

The active strike-slip faults are distributed throughout the Altai and are a known source of large magnitude earthquakes. Modern examples, labelled on Fig. 1a, are the 1931 M_s 8.0 Fu-Yun earthquake in the SW Altai (Baljinnyam et al., 1993) and the 2003 M_w 7.2 Chuya earthquake in the NW part of the range (Nissen et al., 2007). Clear prehistoric ruptures are observed on many other faults (Khil'ko et al., 1985; Baljinnyam et al., 1993; Walker et al., 2006), their long-term preservation enhanced by the cold, semi-arid climate and sparse population.

To date, the only quantitative slip-rates in the Altai are from Vassallo (2006) and Nissen et al. (2009). Vassallo (2006) established minimum horizontal rates of ~0.5 mm yr^{-1} and ~1.2 mm yr^{-1} along the northern and southern Ölgiy-Hovd fault, based on cosmogenic

^{10}Be dating (Fig. 1a). Nissen et al. (2009) used OSL to determine vertical displacement rates of ~0.15–0.35 mm yr^{-1} across thrusts bounding Baatar Hyarhan in the eastern Altai.

2.1. Overview of the Har-Us-Nuur fault

Around 500 km long (~45°–50° N), the Har-Us-Nuur fault trends NNW–SSE through relatively low terrain along the eastern margin of the Altai, adjacent to the Depression of Great Lakes (Fig. 1a). At its northern end f(~46°–50° N), the fault splits into a number of parallel strands. The westernmost of these, the Jid fault, was studied in detail by Walker et al. (2006). They described an en echelon, left-stepping arrangement of partially-infilled tension fissures, caused by the most recent earthquake here. The age of the earthquake was bracketed at 870–980 years from OSL dating of trench material; slip of ~5 m was determined from the size and orientation of the fissures; and the rupture length was estimated at ~90 km. Using earthquake scaling relationships, the authors estimated a moment magnitude of ~7.4.

Khil'ko et al. (1985) described similar ruptures along part of the southernmost Har-Us-Nuur fault, also known as the Tonhil fault (45°–46° N). The estimated coseismic slip (~2.5 m) and rupture length (~25 km) are consistent with a moment magnitude of ~6.9. Although not actually dated, these ruptures were tentatively assigned an age of 500–1000 years by the authors.

In contrast with the northern and southern sections, the central part of the Har-Us-Nuur fault (~46°–49° N) has until now been overlooked, despite it representing an important source of seismic hazard for Hovd (the largest town in western Mongolia, ~50 km to the west). We focussed on the area south of Har-Us-Nuur lake (~47.5°–48° N), where a major restraining-bend — introduced by a change in fault strike — has uplifted the ~3800 m-high Jargalant-Nuruu massif (Fig. 1b). The Har-Us-Nuur fault bounds the eastern margin of these mountains.

3. Late Quaternary slip-rate

3.1. Site descriptions and offsets

South of Har-Us-Nuur lake, the Har-Us-Nuur fault beheads a series of alluvial fans deposited along the eastern margin of the Jargalant-Nuruu massif (Fig. 2). Streams exiting the range bend sharply northwards toward Har-Us-Nuur lake, which constitutes the local base-level. In the northern part of this section, 15 m-pixel Advanced Spaceborne Thermal Emission and Reflection Radiometer (ASTER) and 2.5 m-pixel Satellite Pour l'Observation de la Terre (SPOT-5) images show six light-coloured fan systems sourced from granitic bedrock in the interior part of Jargalant-Nuruu (Fig. 2). Within these systems, incised, abandoned fan surfaces have been displaced right-laterally from the catchment outlets that fed them. The elevation of the range-front increases southwards so these displacements are in an uphill direction and can only have been caused by dextral slip on the Har-Us-Nuur fault. Sourced from granitic bedrock, the displaced surfaces are quartz-rich and thus an obvious target for exposure dating with cosmogenic ^{10}Be.

We visited each of these alluvial fan systems during fieldwork in Summer 2006. From north to south, we refer to them as A–F (Fig. 2b). Detailed SPOT images of individual systems are shown in Figs. 3–5. Most systems contain an active fan (labelled A1, B1 *etc.*), although the youngest surface in the southernmost system (F1) shows minor incision by the active channel (Fig. 5). In contrast, the older, abandoned set of surfaces — A2, B2 *etc.* — are crossed by networks of incised runnels. These channels, up to a few metres wide and one or two deep, contain dark material sourced from mafic bedrock along the adjacent range-front. In fan system F, the eroded remnants of two even older surfaces (F3 and F4), with deeper and wider runnels, are also preserved (Fig. 5).

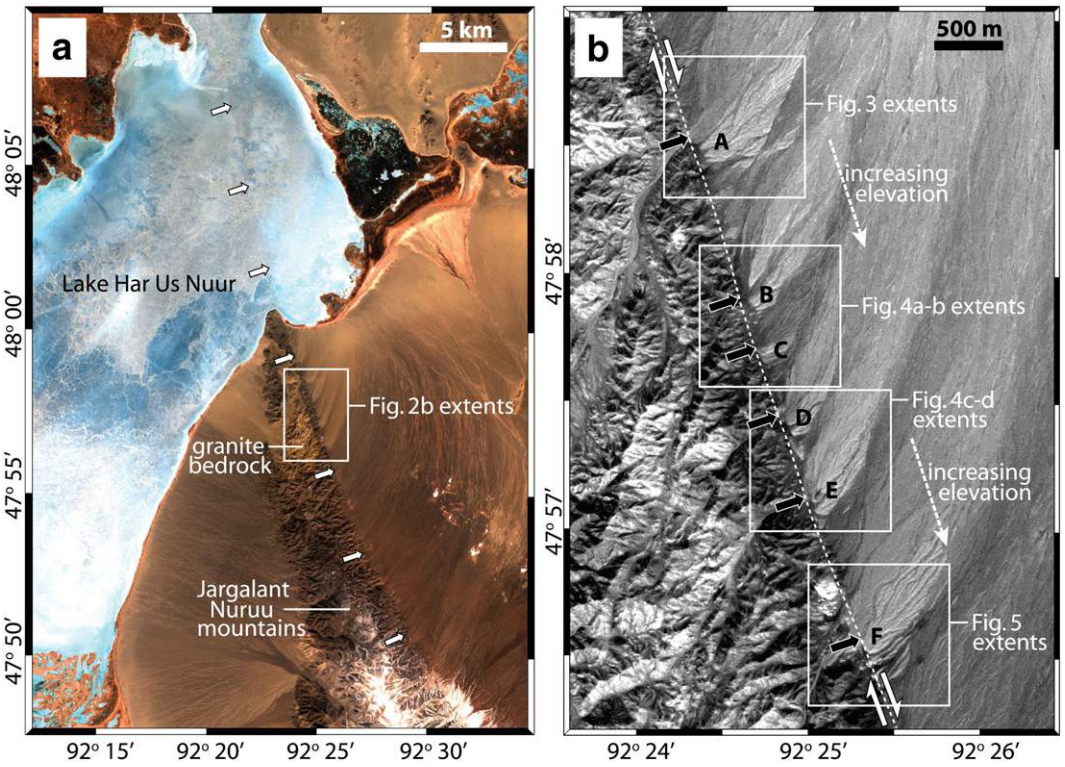

Fig. 2. (a) ASTER image (15 m resolution) of the Har-Us-Nuur fault (picked out by white arrows) just south of the Har-Us-Nuur lake. In the northern part of the image the lake is completely frozen through, and the fault can be made out as it crosses the lake bed. Because there is no topography associated with the fault here, its 166° strike represents the fault slip vector. (b) SPOT-5 image (2.5 m resolution) of a series of six light-coloured alluvial fan systems — labelled A to F — that have been deposited along the eastern margin of the Jargalant-Nuruu mountains. The range-front outlets of the catchments feeding these fans are denoted by black arrows, and the trace of the Har-Us-Nuur fault by a dashed white line.

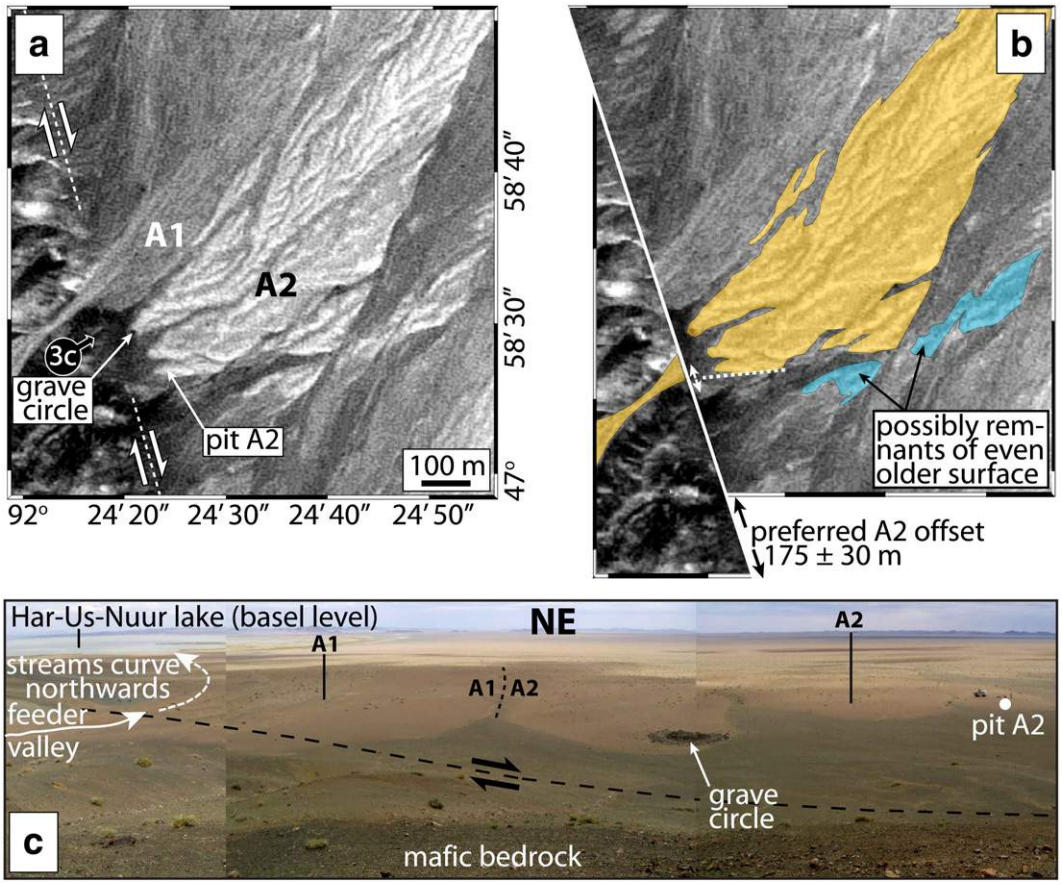

Fig. 3. (a) SPOT-5 image of fan system A. A1 is a younger and slightly darker surface, and is still being deposited by the active stream channel. A2 is older and lighter, and is crossed by several runnels filled with dark material shed from mafic bedrock along the range-front. (b) Reconstruction made by aligning the southern edge of A2 with the southern edge of the feeder valley. The white dotted line shows the extrapolation of the southern margin of A2 back to the fault. The white arrow represents the ±30 m error margin we assign to the preferred, 175 m displacement, reflecting the uncertainty involved in this extrapolation. (c) Panoramic photographs facing ~ NE from 47° 58′ 28″ N 92° 24′ 16″ E. Mafic bedrock can be seen in the foreground; material eroded from this has been washed into the runnels crossing A2.

Away from the runnels the A2–F2 fan surfaces are typically composed of gravel-sized clasts, although there are rare boulders up to ~50 cm in diameter. The surface tops are planar in form and the occasional boulders are coated with desert varnish, except for the lowest few centimeters of exposure which are varnish free. These observations are consistent with only minor erosion of the surface tops. In the SPOT images, the older surfaces all appear lighter in colour than the younger set (Figs. 3–5). This colour difference may reflect weathering or soil development over time, or, alternatively, a systematic change in sediment supply between one period of aggradation and the next (with older fans containing higher proportions of granitic material than younger ones).

The older set of surfaces (A2–F2) all show right-lateral offsets from the catchment outlets that supplied them. However, measuring these displacements is not trivial, because the extents of each fan may have been altered by erosion since they were originally deposited. This is of particular concern for B2, which appears as several, separate patches (Fig. 4a), and C2, D2 and E2, whose margins are not always clearly delineated from surrounding material (Fig. 4b–d). Instead, we focus on quantifying the offsets of A2 and F2, which are relatively extensive and easily distinguishable from surrounding sediment (Figs. 3 and 5); these fans were also targeted for dating (sections 3.2 and 3.3). The extents of A2 and F2 are still likely to have been altered by erosion since deposition, particularly along their northern margins, which are exposed to the active feeder streams. We therefore focus on reconstructing their southern margins (which are probably more intact), estimating displacements relative to the southern edges of the feeder valleys at their outlets.

The southern margin of A2 is visible only to within ~50 m of the fault; closer than this, the A2 fan is masked (or has been eroded) by darker, mafic material shed from the range-front (Fig. 3a, c). To estimate the A2 displacement, we first extrapolate its southern margin back to the fault (white dotted line, Fig. 3b). To restore this margin against the southern edge of the feeder valley requires a displacement of 175 m. We assign error margins of ±30 m to this figure, to reflect the uncertainty in extrapolating the southern margin of A2 back to the fault (Fig. 3b). The displacement of A2 is thus estimated to be 175 ± 30 m.

The precise extents of F2 are also unclear close to the fault. West of the fault, on the southern side of the feeder valley, we interpret a small patch of older material as belonging to F2, but we cannot precisely constrain its southern edge (Fig. 5a,c). This leads to an uncertainty in where to assign the southern edge of the feeder catchment. Equally, a small pressure ridge disguises the precise location of the southern margin of F2 on the eastern side of the fault. We estimate the displacement of the southern margin of F2 to be 140 ± 40 m, with the error bounds reflecting these uncertainties.

Our estimated displacements for A2 and F2 agree to within error. Furthermore, restoring the other abandoned fans (B2–E2) using a ~160 m displacement — consistent with the bounds for A2 and F2 — gives rise to plausible reconstructions (Fig. 4b, d). The offsets are therefore consistent with the contemporaneous deposition of all six surfaces. This implies that periods of fan-building are controlled by climate, which is unlikely to vary significantly over the small geographical area and narrow elevation range (~1275–1400 m) represented by the fan systems. A close relationship between climate

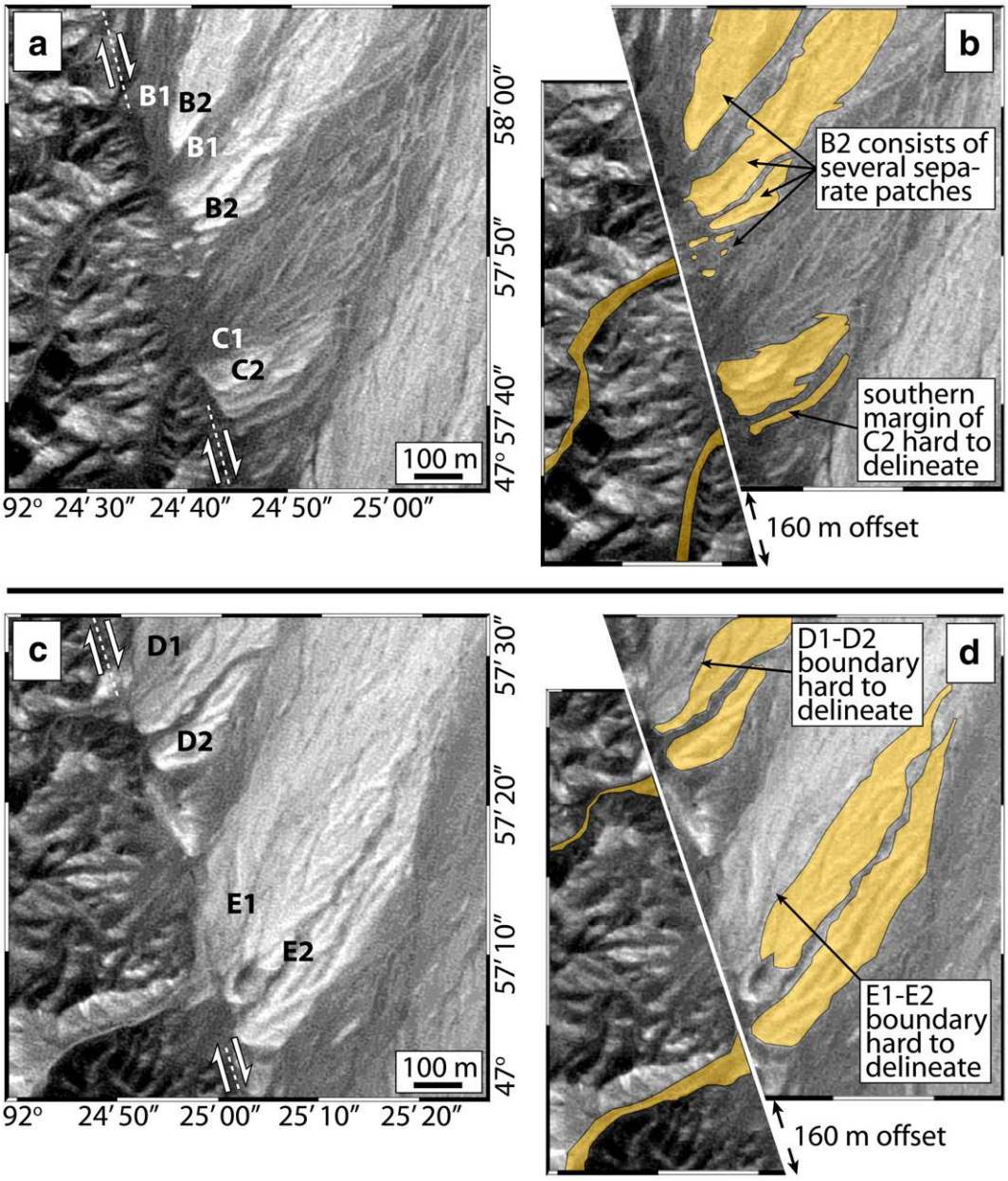

Fig. 4. (a) SPOT-5 image of fan systems B and C. (b) Reconstruction of the B2 and C2 surfaces using a 160 m offset, consistent with both A2 and F2 fans. (c) SPOT image of fan systems D and E. (d) Reconstruction of the D2 and E2 surfaces using a 160 m offset.

and periods of alluvial fan deposition and abandonment is also observed in the Gobi-Altai range, where pulses of fan aggradation — correlated over areas many tens of kilometers wide — were promoted at the transitions from cold, dry, glacial periods to warmer, wetter interglacials (Vassallo et al., 2005; Ritz et al., 2006).

On the southernmost fan system we also observe some younger displacements. Firstly, a clear scarp is preserved across F1, along the line of the fault (Fig. 5a). Secondly, the riser between F1 and F2 preserves a right-lateral displacement along the fault (Fig. 6c). This offset is much smaller than the overall ~140 m displacement of the southern edge of F2 (Fig. 5b); the riser must have been refreshed F2 abandonment, and we assume that the offset dates from F1 abandonment, instead.

To measure these displacements, we constructed a digital elevation model (DEM) of fan system F using differential GPS (Fig. 6a). From a series of elevation profiles through this DEM (e.g. Fig. 6b), the vertical offset across the scarp is 0.4–0.8 m. Parallel profiles taken either side of the fault across the F1–F2 riser show an apparent dextral offset of 12 ± 2 m (Fig. 6d). However, these profiles also show that the riser is steeper on the eastern side of the fault (profile C–D) than on the western side (E–F). This suggests that the riser was refreshed more recently on the eastern side, giving rise to an additional uncertainty in the slip-rate derived from this offset (section 3.5).

3.2. In situ-produced cosmogenic ^{10}Be exposure dating

To calculate the Har-Us-Nuur fault slip-rate, we constrained the timing of alluvial fan abandonment using exposure dating with *in situ*-produced cosmogenic ^{10}Be (Nishiizumi et al., 1986). This rare, long-lived isotope is generated within surficial quartz grains by interactions with cosmic rays. Its production rate is a function of latitude and altitude, and also decreases exponentially with overlying mass so that at depths of a few metres negligible amounts are generated. After a quartz-bearing rock is exposed its ^{10}Be content will increase over time until eventually a steady-state equilibrium between production and decay (plus loss through erosion) is reached

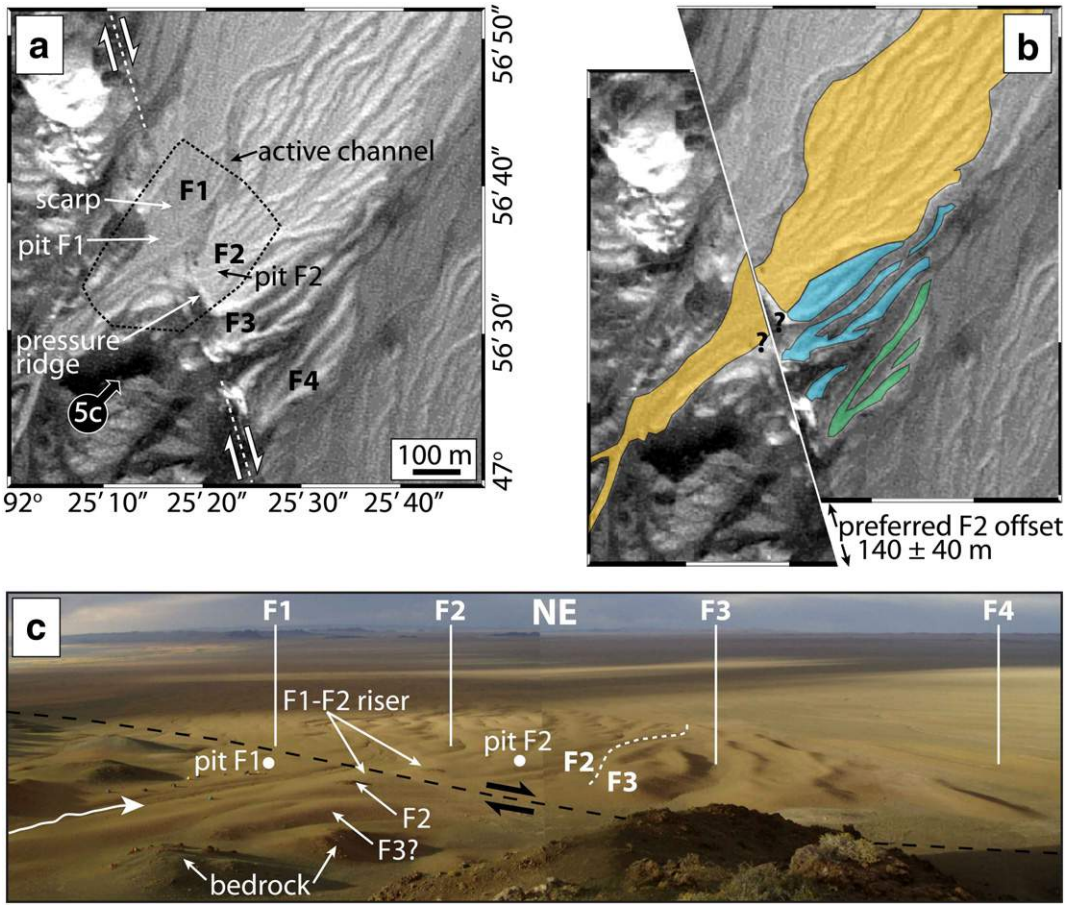

Fig. 5. (a) SPOT-5 image of fan system F. The dashed black line marks the extents of the DEM in Fig. 6a. The faint, dark line crossing the F1 surface is the fault scarp described in section 3.1. (b) Reconstruction based on restoring the southern margin of F2 next to the southern edge of the feeder valley using a displacement of 140 m. The question marks represent the uncertainties in the outline of the southern edge of F2, on either side of the fault. Because of these uncertainties, we assign ±40 m error bounds to the preferred F2 displacement. (c) Panorama facing ~ NE from 47° 56′ 25″ N 92° 25′ 10″ E. Tents in left of picture provide scale.

(Lal, 1991). Providing this equilibrium is not yet achieved, measurements of ^{10}Be concentrations can therefore be used to establish the age at which the rock was exposed. This method has become an important way of determining the timing of alluvial fan abandonment in arid, mountain environments where organic material (for ^{14}C dating) or fine-grained sediment (for luminescence dating) is often unavailable (Ritz et al., 1995).

The ^{10}Be contained in any one quartz grain may include a significant portion obtained prior to deposition — during hillslope exhumation and transport within the catchment area — and the age of fan abandonment can be over-estimated if this inherited component is not recognized (Anderson et al., 1996). There are two methods by which this can be done. In the first, samples are taken from the bed of the active feeder stream, which is not yet abandoned and whose ^{10}Be concentration is effectively derived entirely from pre-depositional exposure. These measurements are then used to correct for the concentrations of individual boulders sampled from the surface of the alluvial fan (Brown et al., 1998). This approach relies on an assumption that the pre-depositional history of clasts in the active channel is similar to that of the material making up the older, abandoned surfaces. As such, this method may be unsuitable for the Jargalant-Nuruu fans, where erosional conditions during fan deposition were probably more intense than at present.

A second strategy involves samples being taken not just from the surface, but from several depths within the deposit to be dated (Repka et al., 1997). In this method, each sample should consist of many separate, small clasts so that individual clast exposure histories are averaged. Providing there is no significant variation in inherited ^{10}Be over time, concentrations should decrease exponentially with depth. The average inherited component is then determined from the asymptotic value that the profile tends to at depth.

In addition to the inherited ^{10}Be, one must also account for any surface erosion the deposit has undergone between deposition and the time of sampling. A high surface erosion rate equates to an increased level of shielding in the past, and will act to reduce the ^{10}Be content of the material now exposed. If the surface erosion rate is unknown, a minimum exposure age can be established by assuming no erosion. Otherwise the erosion rate can be estimated by comparing the shape of vertical profiles of ^{10}Be with theoretical curves calculated with known erosion rates (Siame et al., 2004; Ritz et al., 2006).

In this study we targeted A2, F1 and F2 for exposure dating, using the vertical distribution of ^{10}Be, averaged (at each depth) over many clasts. A 2 m-deep sampling pit was excavated on each surface, at a location carefully chosen to avoid signs of recent erosion or deposition — in particular the runnels on A2 and F2, and the active stream incising into F1 (as well as some small debris flows that overtopped this channel). We measured ^{10}Be concentrations for eight samples (each comprising >100 clasts) from each pit, at 25 cm intervals from the surface down to 1.75 m. The sample locations, sampling procedure, sample preparation, and AMS measurements, are described in detail in the Appendix. Final, vertical profiles of ^{10}Be are shown in Fig. 7.

3.2.1. A2 fan

Sediment exposed in the A2 pit comprises angular to sub-angular coarse gravels and pebbles of quartz-rich granite or mafic composition.

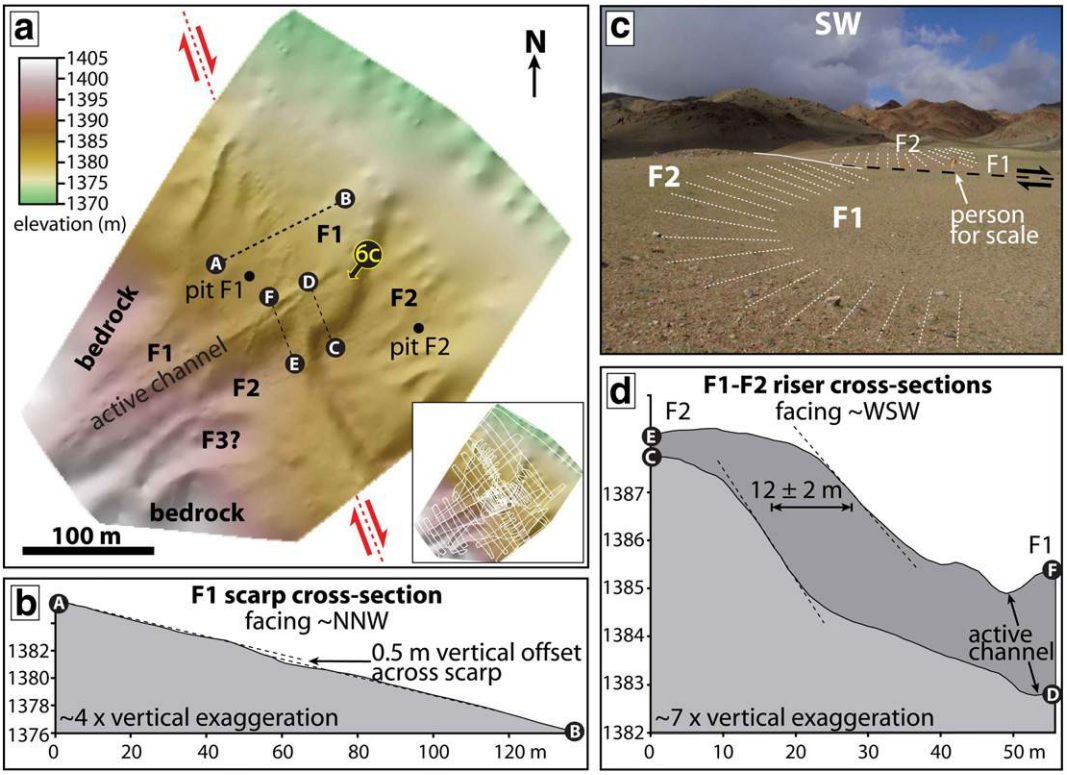

Fig. 6. (a) Digital elevation model (DEM) of fan system F, artificially illuminated from the south-east (a topographic scale is provided in the electronic, colour version of this figure). Its extents are marked on Fig. 5a as a dashed black line. The DEM was made by fitting a surface of minimum curvature to the differential GPS points shown on the inset map. (b) An example of an elevation profile across the scarp on F1. In this case, the surface is displaced, vertically, by 0.5 m; by producing several of these profiles, we bracket the offset at 0.4–0.8 m. (c) Photo facing ~ SW from 47° 56′ 37″ N 92° 25′ 21″ E, showing the F1–F2 riser with a person for scale. (d) Parallel topographic profiles through the F1–F2 riser, taken either side of the fault. The steepest part of the riser (picked out by a dashed line) is displaced, right-laterally, by 12 ± 2 m.

The material is uncemented and shows only subtle stratification, although there is a clear layer of soft sand with occasional pebbles exposed in one pit wall at 50–70 cm depth (we use this fine-grained material for OSL dating in section 3.3).

Averaged ^{10}Be concentrations decrease from ~12×10^5 at g^{-1} at the surface down to ~4×10^5 atoms g^{-1} at a depth of 125 cm, but then rise to ~7×10^5 atoms g^{-1} for the 150 cm and 175 cm samples (Fig. 7a). The pit was situated close to the southern edge of the fan, and we probably excavated through A2 into an older deposit below, from which this final pair of samples was taken. There is no well-developed paleosol at the boundary of these two layers (at 125–150 cm); if our interpretation is correct, this suggests that the surface of the older deposit was removed when the younger material was deposited.

To determine the A2 exposure age we used a chi-squared inversion that minimises the difference between observed ^{10}Be concentrations and vertical profiles predicted by theory (Siame et al., 2004). Details of this technique, together with the values we used for the production rates, attenuation lengths, decay constant, and sediment density, are provided in the Appendix. We assumed that the deepest pair of samples belong to an older deposit, and used only the upper six samples in the inversion. In addition, material collected from the surface may have a more complex history than buried clasts (for instance, they are more likely to have been disturbed through bioturbation), so we also halved the weighting given to the 0 cm sample.

We began by assuming a zero surface erosion rate and, testing a range of values for the inherited ^{10}Be component, solving for the best-fit exposure age. Assuming zero inheritance yielded an age of 93.6 ka but with a poor fit to the data (dotted line, Fig. 7a). The best match between observed and modelled concentrations, satisfying the 1σ analytical errors of all six samples, is for an inheritance of 1.40×10^5 atoms g^{-1} and an age of 74.1 ka (solid line, Fig. 7a). Finally, we tested an inheritance of 4.0×10^5 atoms g^{-1}, which is the value we estimate for the younger, F1 fan (see below). This provided an age of 38.1 ka but with a poor fit to the data (dashed line, Fig. 7a).

Next, using our best-fit value for the inherited ^{10}Be component (1.40×10^5 atoms g^{-1}), we modelled the data again but with the erosion rate now free to vary. The best match between observed and modelled concentrations (with a marginally lower χ^2 value than for no erosion) is for an erosion rate of 2.5 m Ma^{-1} and an age of 80.7 ka; this model distribution lies very close to the 74.1 ka profile and so is not plotted separately on Fig. 7a. A good fit to the data can also be achieved at even greater ages, using higher erosion rates. This is demonstrated by a contour plot of χ^2 values for a range of ages and erosion rates (Fig. 7b); the pronounced trough of low χ^2 values demonstrates a strong trade-off between the two parameters. However, because only small amounts of erosion are likely to have occurred (section 3.1), we consider the original model age of 74.1 ka to be close to the true age, eventhough it formally represents a minimum value.

3.2.2. F1 fan

In general, sediment exposed in the F1 pit closely resembles that of A2. Also like A2, a layer of soft sand is exposed in one of the F1 pit walls, at a depth of 80–90 cm. The F1 pit also contains a distinctive layer of larger cobbles, up to ~10 cm in diameter, at 30 cm depth.

F1 shows no clear decrease in ^{10}Be concentrations with depth, and all but one measurement falls close to 4×10^5 atoms g^{-1} (Fig. 7c). This implies that levels of ^{10}Be are dominated by the inherited component, with only small amounts of additional ^{10}Be produced since deposition. This inherited component is likely to be around 4×10^5 atoms g^{-1}, significantly higher than the value of 1.40×10^5 atoms g^{-1} estimated for A2.The catchment areas of the A and F fan systems are similar in size and elevation; this discrepancy therefore suggests that hillslope

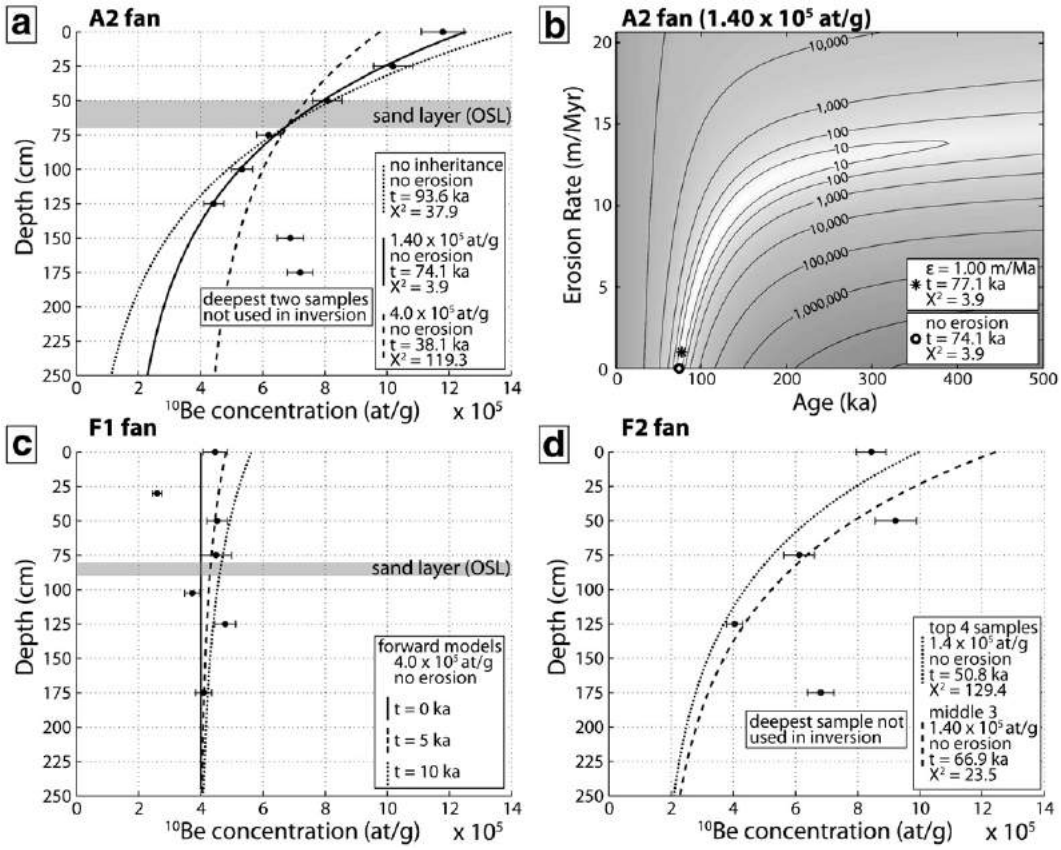

Fig. 7. (a) Vertical profile of ^{10}Be concentrations (averaged over many clasts) through the A2 fan, with horizontal bars showing analytical errors at the 1σ level. The curved lines represent modelled distributions, under the assumption of no erosion and discounting the lowest two samples (see text for details). (b) Plot of χ^2 values for a range of erosion rates and ages, using the best-fit inherited ^{10}Be concentration of 1.40×10^5 atoms g^{-1}. The curved trough in χ^2 values demonstrates a trade-off in χ^2 between age and erosion rate. The circle represents the minimum age (using no erosion); the asterisk represents the overall best-fit age and erosion rate. (c) Vertical profile of ^{10}Be through the F1 fan. Although we do not model this data, we do show forward-modelled distributions for ages of 0 ka, 5 ka and 10 ka. (d) Vertical profile of ^{10}Be through the F2 fan. Curved lines represent best-fit modelled distributions for an inherited component of 1.40×10^5 atoms g^{-1} and assuming no erosion; for the dotted line, the shallowest four samples were used, while for the dashed line, only the middle three samples were used.

erosion rates were lower and/or transport times longer during F1 deposition than for during A2 deposition. The anomalously low concentration in the 30 cm sample may reflect the unusually large size (and presumably shorter transport times) of clasts within this particular horizon.

F1 is clearly younger than A2 or F2, but analytical errors are too large and the data too scattered (even discounting the 30 cm sample) for us to precisely constrain its age. Fig. 7c shows forward-modelled ^{10}Be profiles, for ages of 0 ka, 5 ka and 10 ka, each with an inheritance of 4.0×10^5 atoms g^{-1}. The relatively poor fit of the 10 ka curve implies a younger age, but the scatter in the data is too high to provide firm constraints.

3.2.3. F2 fan

Material in the F2 pit is somewhat finer grained than in A2 or F1, comprising angular to sub-angular gravels with rare cobbles. Like the other pits the sediment shows only subtle stratification, with no clear paleosols. Clasts are again either mafic or granitic, but the latter material contains abundant K-feldspar and is less quartz-rich than granite clasts in the other pits (presumably reflecting the variability of the granitic source in Jargalant-Nuruu).

Only five of the F2 samples yielded measurable ^{10}Be concentrations (Fig. 7d). These vary from ~4×10^5 atoms g^{-1} up to ~9×10^5 atoms g^{-1}, but there is no simple, exponential decay with depth (as there is for A2). To start with, we modelled the shallowest four samples under an assumption of no erosion. Because F2 is probably contemporaneous with A2, and because the two fans are close geographically and in elevation, we also assume an inheritance of 1.40×10^5 atoms g^{-1}, which is the best-fit value for A2. This yielded a best-fit age of 50.8 ka (dotted line, Fig. 7d). By discounting the surface sample, which is most likely to have been contaminated or disturbed (e.g. by bioturbation), a much-improved fit was found for the middle three samples, corresponding to an age of 66.9 ka (dashed line, Fig. 7d). This figure is close to the 74.1 ka age for A2; however, because of the overall scatter in the F2 profile we use the modelled profiles as approximate guides only, and prefer not to assign F2 a formal exposure age.

The ^{10}Be profiles from A2 and F1 suggest only small variations in inheritance (averaged over many clasts) within any one episode of fan aggradation. The large scatter in F2 ^{10}Be concentrations is therefore best explained by pulses of fan-building, with at least three separate stages of aggradation. There are no well-developed paleosols in the F2 pit; however, as we suggest for A2, any soil that developed following an earlier stage of fan-building may have been eroded when the next pulse of sediment was deposited.

3.3. Optically stimulated luminescence (OSL) dating

Optically stimulated luminescence (OSL) provides an alternative and independent method of determining the age at which quartz-bearing sediments were deposited (e.g. Huntley et al., 1985). Subjected to natural radioactivity, electrons within quartz grains are displaced from their position within the mineral lattice and become stored in nearby lattice defects. These trapped electrons are released during prolonged exposure to sunlight, but can begin to accumulate once the grains are buried. Stimulating samples of buried quartz with light in the laboratory releases the trapped electrons together with photons ('luminescence').

By comparing this natural OSL with the luminescence signals produced after the material is given known laboratory radiation doses, the total radiation received during burial (or 'equivalent dose,' D_e) can be established. Meanwhile the dose rate received during burial is determined using measurements of radioactive U, Th and K in the surrounding sediment and from estimates of cosmic radiation. The age at which the sediment sample was last exposed to sunlight is then calculated by dividing the equivalent dose by the dose rate.

Fine-grained aeolian or fluvial sediments are preferred for OSL dating, because they are more likely to have undergone prolonged exposure to sunlight during transport, thus resetting the luminescence clock prior to deposition; if the grains were not fully bleached before burial then the true age of deposition can be over-estimated. The coarse gravels and pebbles within our three ^{10}Be sampling pits are therefore a poor choice of material for OSL dating. However, the A2 and F1 pits each contain a lens-shaped layer of homogeneous, soft sand, exposed on one pit wall (at depths of 50–70 cm and 80–90 cm, respectively). We interpret these as having been deposited by small, low-energy streams within the fan systems. If this interpretation is correct then grains probably underwent significant exposure to sunlight during transport, opening up the possibility of dating their burial with OSL.

We collected three samples from these sand layers — two from A2 and one from F1 — for quartz OSL dating. The dose rate received during burial was calculated using estimates of the cosmic-ray dose rate and from measurements of radioactive U, Th and K. All sampling and laboratory procedures are outlined in the Appendix. For each sample, OSL was measured for between 11 and 14 aliquots; individual D_e values (in Grays) are plotted in Fig. 8 together with an overall probability density function. Weighted mean D_e values and dose rates are shown in Table 1.

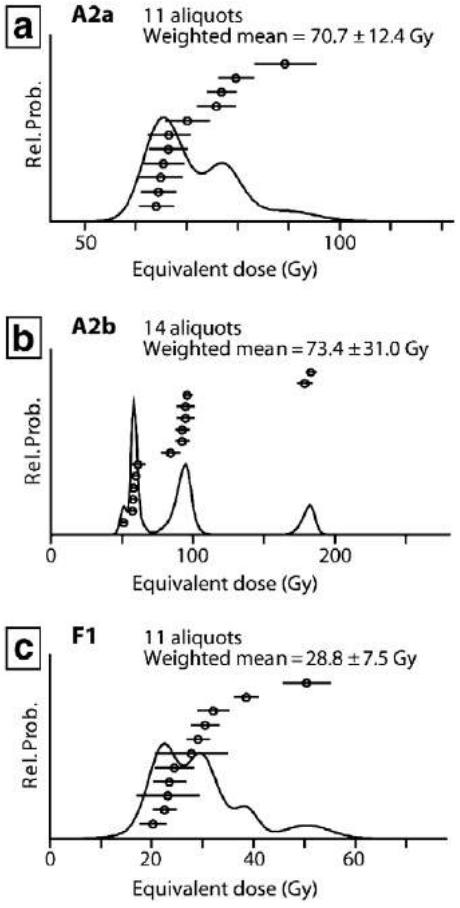

Fig. 8. Equivalent dose distribution plots for OSL samples (a) A2a, (b) A2b and (c) F1. The *x*-axis represents the equivalent dose (D_e, in Grays) required to reproduce the natural OSL signal. D_e values for individual aliquots are displayed in rank order, with an overall probability density function superimposed on top. Error bars in individual aliquot D_e values are based on photon-counting statistics, an error in fitting a straight line through the dose-response plots, and a 1% systematic error.

3.3.1. A2 fan

Two separate samples were collected from the sand layer in the A2 pit. For sample A2a, D_e values agree to within error for seven out of the eleven aliquots, producing a well-defined peak in dose distributions (Fig. 8a). The remaining four aliquots show significantly higher D_e values, suggesting that not all grains were completely reset before deposition. Using the weighted mean D_e, 70.4 ± 12.4 Gy (Table 1), we calculated an age of 18.8 ± 3.5 ka (with 1σ error bounds). If the first peak in dose distributions (~65 Gy) is used (rather than the weighted mean D_e), a lower age of ~17 ka is attained.

D_e values for sample A2b are distributed in three clusters (Fig. 8b). Using the weighted mean D_e, 73.4 ± 31.0 Gy, we calculated an age of 19.8 ± 8.5 ka, consistent with that of A2a. If the higher dose distribution peaks are assumed to represent incompletely bleached sediment, and only the lowest cluster (~60 Gy) used, an age of ~16 ka is attained.

These age estimates are much younger than the minimum exposure age (74.1 ka) calculated from modelling ^{10}Be concentrations from the same pit (section 3.2.1). We discuss possible origins for this discrepancy in section 3.4.

3.3.2. F1 fan

Equivalent doses for F1 aliquots show an even spread from 20 to 32 Gy, except for two aliquots that register higher values (Fig. 8c). Using the weighted mean D_e, 28.8 ± 7.5 Gy, we calculated an age of 6.3 ± 1.7 ka, consistent with the young ages expected from the distribution of ^{10}Be in the same pit (section 3.2.2).

3.4. Discrepancy in A2 age estimates

Before determining the fault slip-rate, we first consider the origin of the discrepancy between the A2 minimum exposure age (74.1 ka) and the A2 OSL ages (18.8 ± 3.5 ka and 19.8 ± 8.5 ka). Besides being crucial for our slip-rate calculations, this discrepancy has implications for other studies in which alluvial deposits are dated with these methods, especially considering that direct comparisons between exposure and luminescence ages are rare (Hetzel et al., 2004; Owen et al., 2006; DeLong and Arnold, 2007). Interestingly, Hetzel et al. (2004) also determine a much younger age using OSL (~50 ka) than with ^{10}Be (~90 ka), for a faulted alluvial fan in the Qilian Shan (China). On the other hand, Owen et al. (2006) and DeLong and Arnold (2007) find OSL ages consistent with those from cosmogenic radionuclides for fans in the Kunlun Shan (China) and California, respectively.

The calculated exposure age for A2 relies on the assumption that the inherited ^{10}Be component, averaged over many individual clasts, is constant within the six samples used in the inversion. If there was a fluctuation in this component as the fan was deposited, then the true exposure age could be different from the value provided by our modelled distribution. However, ^{10}Be concentrations in the younger, F1 fan suggest that the average inheritance remained relatively

Table 1
Weighted mean equivalent doses (D_e), radioactive K, U and Th concentrations, cosmic dose rates, total dose rates and the resulting OSL ages for two samples from the A2 sampling pit and one from the F1 sampling pit.

	A2a	A2b	F1
D_e (Gy)	70.7 ± 12.4	73.4 ± 31.0	28.8 ± 7.5
K (%)	2.81 ± 0.03	2.85 ± 0.03	2.51 ± 0.03
U (ppm)	1.70 ± 0.05	1.40 ± 0.05	4.30 ± 0.05
Th (ppm)	5.60 ± 0.17	5.30 ± 0.17	11.80 ± 0.17
Cosmic dose rate (Gy/ka)	0.252 ± 0.135	0.252 ± 0.135	0.243 ± 0.135
Total dose rate (Gy/ka)	3.76 ± 0.18	3.70 ± 0.18	4.55 ± 0.18
Age (ka)	18.8 ± 3.5	19.8 ± 8.5	6.3 ± 1.7

All errors are shown at the 1σ level.

constant during the course of F1 deposition. A significant fluctuation in inheritance during A2 deposition is therefore unlikely, and we consider the minimum exposure age of 74.1 ka to be robust.

The alternative interpretation for the discrepancy, which we consider more likely, is that we have under-estimated the A2 burial age using OSL. We can think of four possible explanations, outlined below.

The first possibility is that sediment was partially bleached after burial. Severe burrowing by animals could potentially achieve this; however, in each of the sampling pits the stratigraphy appears intact, making this scenario unlikely. During sampling itself, only the ends of the sampling tube could have undergone any exposure. We cannot rule out the possibility that sediment shifted within the sampling tubes during transport — such that bleached grains at the tube ends were mixed in with the pristine material in the central part of the tubes, which was used for the OSL measurements. However, measures were taken to minimise such mixing (Appendix) so this explanation is also improbable.

A second option is that measurements of radioactive K, U and Th within our samples — from which the dose rate received during burial was estimated — are unrepresentative of the sediment as a whole. However, dose rates from A2a and A2b are consistent with one another, making this explanation unlikely.

A third possibility is that an OSL signal from a thermally-unstable feldspar component was measured (along with the quartz OSL) during sample stimulation, leading to OSL age underestimation. Our samples were initially rich in feldspar and although we followed rigorous procedures to isolate quartz (Appendix), a small fraction of feldspar may have remained. A high background OSL observed in the last seconds of typical stimulation cycles (Appendix) is consistent with this scenario, although too few grains were left following quartz isolation for us to conclusively establish (or rule out) feldspar contamination with further tests on the same samples. We note that a similar explanation was considered by Hetzel et al. (2004) to account for their young OSL age, although the authors did not further investigate their age discrepancy.

Even if the quartz signal was successfully isolated, there is one further possible origin for the young OSL ages. Quartz samples from mountain environments in which grains have experienced rather limited environmental histories have sometimes shown abnormal OSL characteristics, including low thermal stability, which can result in age underestimation when standard OSL methodology is used (Klasen, 2008). We also note that Owen et al. (1999) found low quartz sensitivities in sediment samples from the Gobi-Altai (southern Mongolia), suggesting that there may be a regional-scale problem using standard protocol OSL.

Unfortunately, because only a small amount of quartz was left following laboratory quartz isolation procedures, we were unable to follow up the last two possibilities with further tests. However, we will collect more samples from A2 in the future, and use these to investigate the origin of the young OSL ages in more detail.

3.5. Slip-rate

To calculate the slip-rate, we divided the displacement of the A2 fan (175 ± 30 m) by our preferred A2 age (74.1 ka). This yielded a horizontal (right-lateral) slip-rate of 2.4 ± 0.4 mm yr^{-1}. Formally this is a maximum slip-rate as it is based on a minimum exposure age, calculated under an assumption of no erosion. However, the true age is probably close to the minimum age (section 3.2.1), so the true slip-rate probably lies close to this formal maximum rate. In the Appendix, we combine this slip-rate with information from prehistoric earthquake ruptures — observed on a nearby section of the fault and described here for the first time — to estimate the earthquake recurrence interval on the central Har-Us-Nuur fault.

Note that if the A2 OSL ages of (~19 ka) were instead used, a horizontal slip-rate of ~9 mm yr^{-1} would be attained. This is greater than the ~7 mm yr^{-1} shortening rate across the whole Altai range (Calais et al., 2003). Considering that there are many other active faults within the Altai, such a high slip-rate is very unlikely. This supports our view that the A2 OSL ages are too young.

We can also estimate horizontal and vertical slip-rates using the displacements measured on fan system F. Assuming the 12 ± 2 m displacement of the F1–F2 riser dates from F1 abandonment, and using the luminescence age for sample F1 (6.3 ± 1.7 ka), we calculate a horizontal slip-rate of 1.3–3.0 mm yr^{-1}, with a preferred value of 1.9 mm yr^{-1}. Although we cannot be certain that the riser was completely reset before F1 abandonment (section 3.1), this figure is consistent with the ~2.4 mm yr^{-1} slip-rate calculated with the A2 exposure age. Finally, dividing the 0.4–0.8 m vertical displacement across the F1 scarp by the 6.3 ± 1.7 ka OSL age provides a vertical slip-rate of 0.05–0.17 mm yr^{-1},with a preferred value of 0.10 mm yr^{-1}.

4. Discussion

We now discuss the onset of movement on the Har-Us-Nuur fault, and investigate implications for the evolution of faulting and topography across the Altai range.

The initiation of strike slip on the Har-Us-Nuur fault is linked to the onset of mountain-building within its restraining bends — including Jargalant-Nuruu within our study area (Fig. 1b). Bedrock samples collected from a transect of this massif contained too little apatite for us to constrain late Cenozoic uplift and exhumation with apatite (U–Th)/He thermochronology (Appendix). However, we can provide a crude measure of the age of the Har-Us-Nuur fault by dividing the cumulative slip by the late Quaternary slip-rate. The fault strikes parallel to the structural trend of the Altai, and there are no clear lithological offsets with which to measure the total strike-slip motion. However, low-lying bedrock exposed around 20 km east of Jargalant-Nuruu is at an elevation of 1500–1600 m, while within the range the peneplain surface is at about 3500 m. This suggests a cumulative throw of ~2000 m across the fault.

At the alluvial fans studied in section 3, the Har-Us-Nuur fault strikes ~162° and has a horizontal slip-rate of 2.4 ± 0.4 mm yr^{-1}. Adjacent to the highest part of Jargalant-Nuruu the fault strikes 148°, giving a shortening component of ~0.5–0.7 mm yr^{-1}. Although we found no clear exposure of the fault in the sides of river valleys exiting the range, the trace of the fault across the range-front topography suggests a dip of ~60°W, giving a vertical displacement rate of ~0.8–1.2 mm yr^{-1} adjacent to the highest part of the range. At this rate, the 2000 m throw on the fault would be achieved in 1.7–2.4 Ma.

Although this is a crude estimate, it is much younger than initial India-related uplift in the Altai region as a whole, which is thought to date from the late Oligocene to Miocene, or ~28–5 Ma (section 2). This implies either that active deformation migrated to the Har-Us-Nuur fault from elsewhere within the range, or that the deforming zone has widened over time. This result agrees with AFT analyses which show Pliocene cooling ages at Baatar Hyarhan in the eastern Altai (Vassallo, 2006), but Miocene cooling ages in the interior part of the Chinese Altai (Yuan et al., 2006).

The interior part of the Altai contains more continuous mountainous terrain than along the Har-Us-Nuur fault (Fig. 1a), and is an obvious choice for the focus of earlier deformation. If faults in the range interior are, indeed, older, then they have probably rotated further about vertical axes in order to accommodate overall convergence; this is illustrated by the difference in strike between the 2003 Chuya earthquake in the interior, north-western Altai (~ WNW) and the 1931 Fu-Yun earthquake along the western margin of the range (~ NNW; Fig. 1a). These rotations place older faults in the range interior at a higher angle to the regional convergence direction and gives them a relatively large component of shortening. Topography produced by this dip-slip component in turn increases the normal stresses acting on the faults, promoting the switching of deformation onto younger strike-slip faults with favourable orientations. New faults forming in high areas, where the topography is

already elevated, would need to do more work against gravity in order to accommodate convergence than faults in low-lying regions. This highlights a possible mechanism for the migration or widening of deformation onto faults in low areas at the range margins, such as the Har-Us-Nuur fault.

5. Conclusions

The maximum late Quaternary right-lateral slip-rate of the Har-Us-Nuur fault, along the eastern margin of the Altai range, is ~2.4 mm yr^{-1}. Assuming this figure can be extrapolated over longer periods, the onset of movement on the fault was at ~2 Ma, significantly later than the initial uplift of the Altai in the late Oligocene to Miocene (28–5 Ma). These results suggest that deformation in the Altai has widened over time to incorporate faults at the margins of the range. This might be because older faults in the high, range interior have rotated about vertical axes into orientations that require work to be done against gravity.

Acknowledgments

This work was supported by a NERC studentship to Edwin Nissen and NERC funding of COMET. SPOT imagery was acquired through the OASIS programme. We are very grateful to Dr Tien and Dr Zhang (Chinese Earthquake Administration) for their contributions in the field; to our driver, Baatar; student helpers, Baatar, Buyanaa, Deegii, Esukhei and Jakii; Ganbold (in Hovd); and Chimgee and Altan (in Ulaan Baatar). Owen Green, Derek Preston, Steve Wyatt, Jason Day and Allan Davidson helped in preparing ^{10}Be samples, and we thank Lanny McHargue for calculating normalised measured ^{10}Be/^{9}Be ratios from the raw data. Weighted mean equivalent doses were calculated with the Analyst programme, courtesy of Professor Geoff Duller. Finally, we thank Jean-François Ritz, Conall Mac Niocaill, and two anonymous reviewers for their detailed and constructive comments.

Appendix A. Supplementary data

Supplementary data associated with this article can be found, in the online version, at doi:10.1016/j.epsl.2009.06.048.

References

Anderson, R.S., Repka, J.L., Dick, G.S., 1996. Explicit treatment of inheritance in dating depositional surfaces using in situ ^{10}Be and ^{26}Al. Geology 24, 47–51.

Avouac, J.-P., Tapponnier, P., 1996. Kinematic model of active deformation in Central Asia. Geophys. Res. Lett. 20, 895–898.

Baljinnyam, I., Bayasgalan, A., Borisov, B.A., Cisternas, A., Dem'yanovich, M.G., Ganbaatar, L., Kochetkov, V.M., Kurushin, R.A., Molnar, P., Philip, H., Vashchilov, Y.Y., 1993. Ruptures of major earthquakes and active deformation in Mongolia and its surroundings. Geol. Soc. Am. Memoir 181 62 pp.

Bayasgalan, A., Jackson, J., McKenzie, D., 2005. Lithosphere rheology and active tectonics in Mongolia: relations between earthquake source parameters, gravity and GPS measurements. Geophys. J. Int. 163, 1151–1179.

Brown, E.T., Bourlès, D.L., Raisbeck, G.M., Yiou, F., Burchfiel, B.C., Molnar, P., Deng, Q., Li, J., 1998. Estimation of slip rates in the southern Tien Shan using cosmic ray exposure dates of abandoned alluvial fans. Geol. Soc. Am. Bull. 110 (3), 377–386.

Brown, E.T., Bendick, R., Bourlès, D.L., Gaur, V., Molnar, P., Raisbeck, G.M., Yiou, F., 2002. Slip rates of the Karakorum fault, Ladakh, India, determined using cosmic ray exposure dating of debris flows and moraines. J. Geophys. Res. 107 (B9), 2192.

Burtman, V.S., Skobelev, S.F., Molnar, P., 1996. Late Cenozoic slip on the Talas-Ferghana fault, the Tien Shan, central Asia. Geol. Soc. Am. Bull. 108, 1004–1021.

Calais, E., Vergnolle, M., San'kov, V., Lukhnev, A., Miroshnitchenko, A., Amarjargal, S., Déverchère, J., 2003. GPS measurements of crustal deformation in the Baikal-Mongolia area (1994–2002): implications for current kinematics of Asia. J. Geophys. Res. 108 (B10), 2501.

Chen, Z., Burchfiel, B.C., Liu, Y., King, R.W., Royden, L.H., Tang, W., Wang, E., Zhao, J., Zhang, X., 2000. Global Positioning System measurements from eastern Tibet and their implications for India/Eurasia intercontinental deformation. J. Geophys. Res. 105 (B7), 16,215–16,228.

Cunningham, W.D., 1998. Lithospheric controls on late Cenozoic construction of the Mongolian Altai. Tectonics 17, 891–902.

Cunningham, D., 2001. Cenozoic normal faulting and regional doming in the southern Hangay region, Central Mongolia: implications for the origin of the Baikal rift province. Tectonophys. 331, 389–411.

Cunningham, D., 2005. Active intracontinental transpressional mountain building in the Mongolian Altai: defining a new class of orogen. Earth Planet. Sci. Lett. 240, 436–444.

De Grave, J., Van den haute, P., 2002. Denudation and cooling of the Late Teleskoye Region in the Altai Mountains (South Siberia) as revealed by apatite fission-track thermochronology. Tectonophys 349, 145–159.

DeLong, S.B., Arnold, L.J., 2007. Dating alluvial deposits with optically stimulated luminescence, AMS ^{14}C and cosmogenic techniques, western Transverse Ranges, California, USA. Quat. Geochron. 2, 129–136.

Devyatkin, E.V., 1974. Structures and formational complexes of the Cenozoic activated stage (in Russian). Tectonics of the Mongolian People's Republic. Nauka, Moscow, pp. 182–195.

Devyatkin, E.V., 1981. The Cenozoic of Inner Asia (in Russian). Nauka, Moscow, Moscow.

Engdahl, E.R., van der Hilst, R.D., Buland, R., 1998. Global teleseismic earthquake relocation from improved travel times and procedures for depth determination. Bull. Seismol. Soc. Am. 88, 722–743.

England, P., Molnar, P., 1997. The field of crustal velocity in Asia calculated from Quaternary rates of slip on faults. Geophys. J. Int. 130, 551–582.

England, P., Molnar, P., 2005. Late Quaternary to decadal velocity fields in Asia. J. Geophys. Res. 110, B12401.

Hetzel, R., Tao, M., Stokes, S., Niedermann, S., Ivy-Ochs, S., Gao, B., Strecker, M.R., Kubik, P.W., 2004. Late Pleistocene/Holocene slip rate of the Zhangye thrust (Qilian Shan, China) and implications for the active growth of the northeastern Tibetan Plateau. Tectonics 23, TC6006.

Holt, W.E., Chamot-Rooke, N., Pichon, X.L., Haines, A.J., Shen-Tu, B., Ren, J., 2000. Velocity field in Asia inferred from Quaternary fault slip rates and Global Positioning System observations. J. Geophys. Res. 105 (B8), 19,185–19,210.

Howard, J.P., Cunningham, W.D., Davies, S.J., Dijkstra, A.H., Badarch, G., 2003. The stratigraphic and structural evolution of the Dzereg basin, western Mongolia: clastic sedimentation, transpressional faulting and basin destruction in an intraplate, intracontinental setting. Basin Res. 15, 45–72.

Huntley, D.J., Godfrey-Smith, D.I., Thewalt, M.L.W., 1985. Optical dating of sediments. Nature 313, 105–107.

Jolivet, M., Ritz, J.-F., Vassallo, R., Larroque, C., Braucher, R., Todbileg, M., Chauvet, A., Sue, C., Arnaud, N., De Vicente, R., Arzhanikova, A., Arzhanikov, S., 2007. Mongolian summits: an uplifted, flat, old but still preserved erosion surface. Geology 35, 871–874.

Klasen, N., 2008. Underestimation of quartz OSL ages for glacifluvial sediments from the northern Alpine foreland. LED2008 Conference, Paper O-28.

Khil'ko, S.D., Kurushin, R.A., Kochetkov, V.M., Baljinnyam, I., Monkoo, D., 1985. Strong earthquakes, paleoseismological and macroseismic data (in Russian). Earthquakes and the Basis for Seismic Zoning of Mongolia, Transactions 41, –Mongolian Scientific Geological Research Expedition. Nauka, Moscow, pp. 19–83.

Lal, D., 1991. Cosmic ray labeling of erosion surfaces — in situ nuclide production rates and erosion models. Earth Planet. Sci. Lett. 104, 424–439.

Lasserre, C., Morel, P.-H., Gaudemer, Y., Tapponnier, P., Ryerson, F.J., King, G.C.P., Métivier, F., Kasser, M., Kashgarian, M., Baichi, L., Taiya, L., Daoyang, Y., 1999. Postglacial left slip rate and past occurrence of $M \geq 8$ earthquakes on the western Haiyuan fault, Gansu, China. J. Geophys. Res. 104 (B8), 17,633–17,652.

Liu, Z., Bird, P., 2008. Kinematic modelling of neotectonics in the Persia–Tibet–Burma orogen. Geophys. J. Int. 172, 779–797.

Nishiizumi, K., Arnold, J.R., Lal, D., Klein, J., Middleton, R., 1986. Production of Be-10 and Al-26 by cosmic rays in terrestrial quartz in situ and implications for erosion rates. Nature 319, 134–136.

Nissen, E., Emmerson, B., Funning, G.J., Mistrukov, A., Parsons, B., Robinson, D.P., Rogozhin, E., Wright, T.J., 2007. Combining InSAR and seismology to study the 2003 Siberian Altai earthquakes-dextral strike-slip and anticlockwise rotations in the northern India–Eurasia collision zone. Geophys. J. Int. 169, 216–232.

Nissen, E., Walker, R., Molor, E., Fattahi, M., Bayasgalan, A., 2009. Late Quaternary rates of uplift and shortening at Baatar Hyarhan (Mongolian Altai) with optically stimulated luminescence. Geophys. J. Int. 177, 259–278.

Owen, L.A., Cunningham, D., Richards, B.W.M., Rhodes, E., Windley, B.F., Dorjnamjaa, D., Badamgarav, J., 1999. Timing of formation of forebergs in the northeastern Gobi Altai, Mongolia: implications for estimating mountain uplift rates and earthquake recurrence intervals. J. Geol. Soc. London 156, 457–464.

Owen, L.A., Finkel, R.C., Haizhou, M., Barnard, P.M., 2006. Late Quaternary landscape evolution in the Kunlun Mountains and Qaidam Basin, Northern Tibet: a framework for examining the links between glaciation, lake level changes and alluvial fan formation. Quat. Int. 154–155, 73–86.

Peltzer, G., Saucier, F., 1996. Present-day kinematics of Asia derived from geologic fault rates. J. Geophys. Res. 101 (B12), 27,943–27,956.

Repka, J.L., Anderson, R.S., Finkel, R.C., 1997. Cosmogenic dating of fluvial terraces, Fremont River, Utah. Earth Planet. Sci. Lett. 152, 59–73.

Ritz, J.-F., Brown, E.T., Bourlès, D.L., Philip, H., Schlupp, A., Raisbeck, G.M., Yiou, F., Enkhtuvshin, B., 1995. Slip rates along active faults estimated with cosmic-ray exposure dates: application to the Bogd fault, Gobi-Altaï, Mongolia. Geology 23, 1019–1022.

Ritz, J.-F., Bourlès, D., Brown, E.T., Carretier, S., Chéry, J., Enhtuvshin, B., Galsan, P., Finkel, R.C., Hanks, T.C., Kendrick, K.J., Philip, H., Raisbeck, G., Schlupp, A., Schwartz, D.P., Yiou, F., 2003. Late Pleistocene to Holocene slip rates for the Gurvan Bulag thrust fault (Gobi-Altay, Mongolia) estimated with ^{10}Be dates. J. Geophys. Res. 108 (B3), 2162.

Ritz, J.-F., Vassallo, R., Braucher, R., Brown, E.T., Carretier, S., Bourlès, D.L., 2006. Using in situ-produced ^{10}Be to quantify active tectonics in the Gurvan Bogd mountain range (Gobi-Altay, Mongolia). In Situ-Produced Cosmogenic Nuclides and Quantification of Geological Processes: Geol. Soc. Am. Spec. Papers, 415, pp. 87–110.

Sella, G.F., Dixon, T.H., Mao, A., 2002. REVEL: a model for recent plate velocities from space geodesy. J. Geophys. Res. 107 (B4), 2081.

Sengör, A.M.C., Natal'in, B.A., Burtman, V.S., 1993. Evolution of the Altaid tectonic collage and Palaeozoic crustal growth in Eurasia. Nature 364, 299–307.

Siame, L., Bellier, O., Braucher, R., Sébrier, M., Cushing, M., Bourlès, D., Hamelin, B., Baroux, E., de Voogd, B., Raisbeck, G., Yiou, F., 2004. Local erosion rates versus active tectonics: cosmic ray exposure modelling in Provence (south-east France). Earth Planet. Sci. Lett. 220, 345–364.

Tapponnier, P., Molnar, P., 1979. Active faulting and Cenozoic tectonics of the Tien Shan, Mongolia, and Baykal regions. J. Geophys. Res. 84 (B7), 3425–3459.

Thomas, J.C., Lanza, R., Kazansky, A., Zykin, V., Semakov, N., Mitrokhin, D., Delvaux, D., 2002. Paleomagnetic study of Cenozoic sediments from the Zaisan basin (SE Kazakhstan) and the Chuya depression (Siberian Altai): tectonic implications for central Asia. Tectonophys. 351, 119–137.

Thompson, S.C., Weldon, R.J., Rubin, C.M., Abdrakhmatov, K., Molnar, P., Berger, G.W., 2002. Late Quaternary slip rates across the central Tien Shan, Kyrgyzstan, central Asia. J. Geophys. Res. 107 (B9), 2203.

Van der Woerd, J., Ryerson, F.J., Tapponnier, P., Gaudemer, Y., Finkel, R., Meriaux, A.S., Caffee, M., Guoguang, Z., Qunlu, H., 1998. Holocene left-slip rate determined by cosmogenic surface dating on the Xidatan segment of the Kunlun fault (Qinghai, China). Geology 26, 695–698.

Vassallo, R., 2006. Chronologie et évolution des reliefs dans la région de Mongolie-Sibérie: Approche morphotectonique et géochronologique (in French), Ph.D. Thesis, Université Montpellier 2.

Vassallo, R., Ritz, J.-F., Braucher, R., Carretier, S., 2005. Dating faulted alluvial fans with cosmogenic ^{10}Be in the Gurvan Bogd mountain range (Gobi-Altay, Mongolia): climatic and tectonic implications. Terra Nova 17, 278–285.

Vassallo, R., Ritz, J.-F., Braucher, R., Jolivet, M., Carretier, S., Larroque, C., Chauvet, A., Sue, C., Todbileg, M., Bourlès, D., Arzhannikova, A., Arzhannikov, S., 2007. Transpressional tectonics and stream terraces of the Gobi-Altay, Mongolia. Tectonics 26, TC5013.

Walker, R.T., Bayasgalan, A., Carson, R., Hazlett, R., McCarthy, L., Mischler, J., Molor, E., Sarantsetseg, P., Smith, L., Tsogtbadrakh, B., Tsolmon, G., 2006. Geomorphology and structure of the Jid right-lateral strike-slip fault in the Mongolian Altay mountains. J. Struct. Geol. 28, 1607–1622.

Wang, Q., Zhang, P.-Z., Freymueller, J.T., Bilham, R., Larson, K.M., Lai, X., You, X., Niu, Z., Wu, J., Li, Y., Liu, J., Yang, Z., Chen, Q., 2001. Present-day crustal deformation in China constrained by Global Positioning System measurements. Science 294, 574–578.

Yuan, W., Carter, A., Dong, J., Bao, Z., 2006. Mesozoic–Tertiary exhumation history of the Altai Mountains, northern Xinjiang, China: new constraints from apatite fission track data. Tectonophys. 412, 183–193.